

Mimicking Photosynthesis with Supercomplexed Lipid Nanoassemblies: Design, Performance, and Enhancement Role of Cholesterol

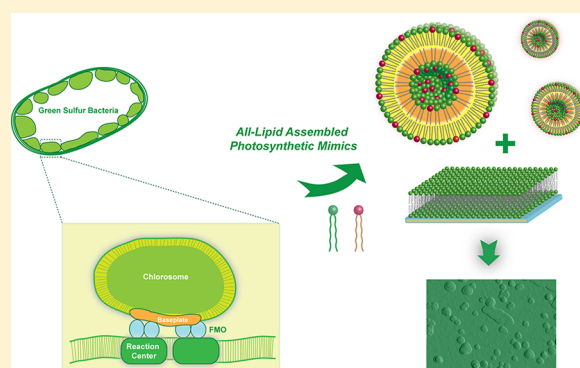
Mingming Wang,[†] Jinquan Chen,^{‡,§} Tianquan Lian,[‡] and Wei Zhan^{*,†}

[†]Department of Chemistry and Biochemistry, Auburn University, Auburn, Alabama 36849, United States

[‡]Department of Chemistry, Emory University, Atlanta, Georgia 30322, United States

Supporting Information

ABSTRACT: We report here a new approach to mimicking photosynthesis that relies on supercomplexed lipid nanoassemblies to organize small organic species for coordinated light harvesting, energy/electron transfer, and photo-to-electrochemical energy conversion. Specifically, we demonstrate efficient photoinduced electron transfer (PeT) between rhodamine and fullerene assembled together via electrostatically bound liposome and lipid bilayer hosts. The remarkable impact of the lipid matrix on the photoconversion efficiency is further revealed by cholesterol, whose addition is found to modify the distribution and organization of the coassembled rhodamine dyes and thus their photodynamics. This significantly expedites the energy transfer (ET) among rhodamine dyes, as well as the PeT between rhodamines and fullerenes. A respectable 14% photon-to-electron conversion efficiency was achieved for this supercomplexed system containing 5% rhodamines, 5% fullerenes, and 30% cholesterol. The morphology, photodynamics, and photoelectrochemical behavior of these lipid supercomplexes were thoroughly characterized using atomic force microscopy (AFM), fluorescence microscopy, steady-state and time-resolved fluorescence spectroscopy, and transient absorption (TA) and photoaction spectroscopy. A detailed discussion on enhancement mechanisms of cholesterol in this lipid-complexed photosynthesis-mimicking system is provided at the end.



INTRODUCTION

The grand scale and harmonious blend of efficiency and sustainability make natural photosynthesis an inexhaustible source for us to learn and develop new approaches to effective solar energy utilization. Although the components and architectures involved in the photosynthetic apparatus vary rather greatly among different species, a general operating scheme exists,^{1–3} in which lipid membrane-bound proteins assemble various pigments and cofactors mostly noncovalently to carry out coordinated energy and charge transfer at specific locations. Through these supercomplexed cross-membrane networks, the harvested light energy is directionally funneled to the charge-separation sites, and the subsequent electron transfer is coupled, for example, in the case of green plants, to proton translocation across lipid membranes to build up proton motive force for biochemical fuel production. To construct robust biomimetic systems following these design principles, however, one immediately faces what may be called the protein paradox. On one hand, a protein-free system is desirable because photosynthetic proteins are fragile and unattainable synthetically, which unfortunately often leads to function loss and compromised performance. To start to address this fundamental issue, we report here a new protein-free, hybrid

mimetic strategy that relies on supercomplexed lipid nanoassemblies to organize small organic species for coordinated light harvesting, energy/electron transfer, and photo-to-electrochemical energy conversion. Owing to their biological significance and versatility in molecular assembling, several lipid structures including liposomes (vesicles)^{4,5} and lipid bilayers^{6,7} have been actively used to mimic various aspects of natural photosynthesis.⁸ Herein, we demonstrate that these lipid building blocks can be further assembled into higher-order architectures to mimic several key processes in photosynthesis with promising efficiency.

One natural system that we have drawn particular inspiration from is green sulfur bacteria (GSB),^{9,10} which are anoxygenic photosynthetic bacteria that have evolved a relatively simple architecture to survive extremely low light conditions. To maximally capture the limited photons available, GSB have developed the largest light-harvesting complex in nature, that is, the chlorosomes,^{11,12} each typically containing >200 000 bacteriochlorophylls (BChls) and carotenoids self-assembled

Received: April 30, 2016

Revised: June 27, 2016

Published: June 29, 2016

into multilamellar tubular aggregates that are wrapped in a monolayer of chlorosome proteins and lipids (Figure 1A).

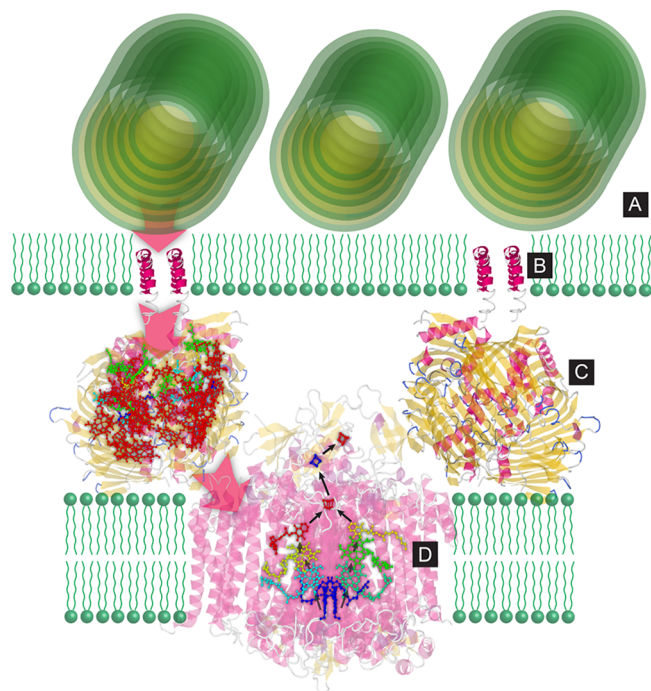


Figure 1. Organization of photosynthetic components in GSB. (A–D): the chlorosome (part), baseplate, FMO protein, and RC. Energy and electron flows are depicted by red and black arrows, respectively.

Within these aggregates, the BChls display a Q_y absorption maximum at 740–750 nm. A quasi-crystalline region called baseplate¹³ (Figure 1B) forms within the monolayer sheath of the chlorosome, which further connects the chlorosome with another photosynthetic component, the Fenna–Matthews–Olson (FMO) protein¹⁴ (Figure 1C), at the bottom. The baseplate primarily comprises protein CmsA and BChl *a* and has a λ_{max} (Q_y) at 790–800 nm, whereas BChls in the FMO complex exhibit peak absorption at \sim 815 nm.¹⁵ The FMO proteins are aqueous-exposed trimers that affix the reaction center (RC, Figure 1D) complex typically by a 2:1 stoichiometry.¹⁶ Together, this four-tier architecture ensures the harvested light energy to be efficiently funneled through an energy transfer (ET) cascade:^{10,11} chlorosomes \rightarrow baseplates \rightarrow FMO \rightarrow RC, and only at the last stop is the light energy converted to electrochemical energy via charge separation and transfer.

Clearly, the success of a protein-free mimicking system depends on how well these sophisticated protein-enabled functions can be replaced or compensated, which, to the minimum, entails a structural scaffold that can organize all involved components into desired locations and facilitate directional energy and electron flows. In this work, we set to explore the potential of supercomplexed lipid nanostructures in filling these roles. Specifically, we have discovered a robust electronic communication between rhodamine and fullerene organized in these lipid nanoassemblies and cholesterol as a significant enhancer of the overall photoconversion efficiency. The structure, performance, and underlying enhancement mechanisms are investigated in detail.

EXPERIMENTAL SECTION

Chemicals. Lipids, including 1,2-dioleoyl-*sn*-glycero-3-phosphocholine (DOPC), 1,2-dioleoyl-3-trimethylammonium-propane (DOTAP), 1,2-dipalmitoyl-*sn*-glycero-3-phosphocholine (DPPC), 1,2-dipalmitoyl-*sn*-glycero-3-phospho-*rac*-(1-glycerol) sodium salt (DPPG), and 1,2-dipalmitoyl-*sn*-glycero-3-phosphoethanolamine-*N*-(lissamine rhodamine B sulfonyl) (ammonium salt) (Rho-DPPE), were purchased from Avanti Polar Lipids (Alabaster, AL). Paraformaldehyde and glutaraldehyde were obtained from Electron Microscopy Sciences (Hatfield, PA). Monomalonic fullerene C_{60} was synthesized according to a procedure described previously.⁷ Other chemicals, including cholesterol, 4-(2-hydroxyethyl)piperazine-1-ethanesulfonic acid (HEPES), (+)-sodium *L*-ascorbate, 1-dodecanethiol, *D*-(+)-glucose, glucose oxidase from *Aspergillus niger*, and catalase from bovine liver, were obtained from Sigma-Aldrich. All solutions employed in this work were prepared using 18.2 M Ω -cm deionized (DI) water (Millipore).

Formation of Two-Tier Lipid Nanoassemblies. The formation of a single lipid bilayer on glass or indium tin oxide (ITO)-coated substrates was achieved by lipid fusion using liposome solutions.⁷ Before the exposure to liposome solutions, the substrates were first sonicated in acetone for 30 min and then boiled with base piranha solution ($\text{NH}_3 \cdot \text{H}_2\text{O}/30\% \text{H}_2\text{O}_2/\text{DI water}$, 1:1:5, v/v) for another 30 min. These substrates were subsequently sonicated in DI water for 10 min, thoroughly rinsed with DI water, carefully dried with an argon stream, and then assembled in Teflon cells for further use.

The preparation of liposomes was carried out using an extrusion-based method.⁷ To start, appropriate quantities of lipids dissolved in chloroform were combined into a 50 mL round-bottom flask and thoroughly dried by rotary evaporation. The resulting thin lipid film on the flask wall was then rehydrated with HEPES buffer (10 mM HEPES, 100 mM NaCl, pH 7.70) by 1 h sonication at a temperature at least 10 °C above the phase transition temperatures (T_m) of the involved lipids. Such lipid suspensions were then extruded consecutively through polycarbonate membranes with 400 and 80 nm pores (Nuclepore, Whatman), again above their T_m . The final concentration of the as-prepared liposomes is typically \sim 2.5 mM. For the preparation of liposomes containing fullerene, membranes of 400 and 200 nm pore sizes were used instead.

To form a lipid bilayer on glass or ITO-coated glass substrates, a 300 μL thus-prepared liposome solution composed of 5% C_{60} , 20% DOTAP, and 75% DOPC (in mole fraction) was gently laid on a freshly cleaned substrate and incubated for 2 h. After that, the unbound liposome was removed by thorough buffer exchange (10 mM HEPES, 100 mM NaCl, pH 7.70). To assemble an additional layer of liposomes onto the above-described cationic lipid bilayer, 200 μL of anionic liposomes (Rho-DPPE/DPPG/DPPC, 5/15/80, or, Rho-DPPE/DPPG/cholesterol/DPPC, 5/15/30/50, in mole fraction) was added into the Teflon cell housing the lipid bilayer and incubated for 1 h. The unattached liposomes were similarly removed from the cell by exchanging with HEPES buffer.

To ensure reproducibility, all subsequent measurements of these two-layer lipid nanoassemblies were conducted on the same day of their preparation.

Fluorescence Microscopy. Fluorescence images of lipid samples deposited on glass substrates were collected on a Nikon A1+/MP confocal scanning laser (561 nm) microscope (Nikon Instruments, Inc., Melville, NY) together with a 595 ± 25 nm emission filter.

Spectroscopy. Absorption spectra of liposome samples containing Rho-DPPE were acquired on a UV–Vis spectrophotometer (Cary 50 Bio, Varian). Steady-state fluorescence spectroscopy data of the two-tier lipid nanoassemblies formed on glass substrates were recorded using a PI Acton spectrometer (SpectraPro SP 2356, Acton, NJ) connected to the side port of an epifluorescence microscope (Nikon TE-2000 U, Japan). The fluorescence signal was recorded using a charge-coupled device (CCD) camera (PI Acton PIXIS: 400B, Acton, NJ) attached to the spectrometer. The excitation was provided by a mercury lamp (X-Cite 120, EXFO, Ontario, Canada) filtered at 475 ± 20 nm; and a long-pass filter with a cutoff wavelength of 561 nm was

used for emission. The obtained spectra are not corrected for distortions due to spectral nonuniformity associated with the filters and CCD camera, which are expected to be small.

Fluorescence lifetimes of rhodamines either suspended in buffer solutions or assembled in the two-tier lipid nanoassemblies were measured using a time-correlated single-photon counting system, which comprises a synchronizer/analyzer (PicoHarp 300, PicoQuant, Germany), a picosecond pulsed diode laser (PDL 800-B, wavelength: 405 nm), and a single-photon counting module (PDM Series, Micro Photon Devices, Italy). In the former case, a quartz fluorometer cell (Sub Micro type, Starna Cells, CA) was used to hold liposome solutions; the final rhodamine concentration in all samples was controlled to be $\sim 0.5 \mu\text{M}$. To be able to capture fluorescence signals emitted directly from the lipid nanoassemblies, this system was further coupled to a fluorescence microscope (Nikon TE-2000U), in which both the laser head and the photon counting module were directly mounted onto the microscope and optically aligned. All lipid samples were formed on glass substrates (Corning, Micro Slide 2947), in which all bottom lipid bilayers contain DOPC/DOTAP in an 80/20 mixing ratio with/without five additional fractions of C_{60} . Throughout the measurements, the laser head was operated at a repetition rate of 10 MHz. According to the manufacturer, this laser produces a minimum pulse width of 59 ps and a power of 29 pJ/pulse. All lifetime data were fitted by the exponential-tail fit method included in the fitting software package, FluoFit (PicoQuant, Germany). Oxygen was removed from all media by purging argon for at least 30 min right before the fluorescence measurements.

Transient absorption (TA) spectra were recorded with a pump-probe spectrometer based on a regenerative amplified titanium-sapphire laser system (Coherent Legend, 800 nm, 150 fs, 2.5 mJ/pulse, and 1 kHz repetition rate). Liposome samples with a total lipid concentration of $\sim 2.5 \text{ mM}$ in HEPES buffer (10 mM HEPES, 100 mM NaCl, pH 7.70) were excited using a pump pulse with a center wavelength of 515 nm obtained by sum frequency generation of the signal from an optical parametric amplifier (Opera, Coherent) and a small portion of ($\sim 7\%$) 800 nm output in a BBO crystal. The absorption variations were probed with a white light continuum from 430 to 750 nm generated by attenuating and focusing an 800 nm pulse into a 1 mm thick sapphire window. The pump and probe beam diameters at the sample were 300 and 150 μm , respectively. The probe beam after passing the sample was collimated and focused into a fiber-optics-coupled multichannel spectrometer with complementary metal-oxide semiconductor (CMOS) sensors and detected at a frequency of 1 kHz. The pump beam was chopped with a synchronized chopper to 500 Hz. The changes in absorbance for the pumped and unpumped samples were calculated. Cuvettes of 1 mm size were used for all spectroscopy measurements. The instrument response function (IRF) of this system was measured to be $\sim 150 \text{ fs}$ by measuring solvent responses under the same experimental conditions.

Atomic Force Microscopy (AFM). The AFM images were obtained either in tapping mode in air on a Veeco atomic force microscope (Dimension 3000) or in a fluid using a Bruker MultiMode 8 atomic force microscope (Bruker, USA) operated in the PeakForce quantitative nanomechanical mapping (PeakForce QNM) mode. In the former measurements, etched Si tips (FM-20, Nanoworld) with a force constant of 2.8 N/m and resonance frequency of 75 kHz were used. The tip scanning was operated at 2 Hz. In-fluid measurements were carried out with two silicon nitride probes (Models: ScanAsyst Fluid, Bruker, 0.7 N/m, 20 nm tip radius; DNP S10, Bruker, 0.24–0.35 N/m, 10 nm tip radius) at a scan rate of 1 Hz and a resolution of 512 pixels \times 512 pixels.

To prepare lipid assemblies suitable for in-air AFM scanning, a modified assembling procedure was followed. First, an alkanethiol self-assembled monolayer (SAM)/lipid hybrid bilayer¹⁷ formed on 10 nm gold-coated glass slides (Sigma-Aldrich) was used as the base layer. To start, these slides were treated with a piranha solution (concentrated H_2SO_4 to 30% H_2O_2 , 3/1, v/v) for 3 min, thoroughly rinsed with DI water, dried under argon, and were then incubated in 1 mM 1-dodecanethiol in ethanol overnight. The excess thiol was removed by rinsing the substrate with ethanol and DI water and finally dried with

argon. To form the hybrid bilayer, a liposome solution (DOTAP/DOPC, 2/8 in mole fraction) of suitable concentration was added onto the SAM and incubated for 2 h. The unbound liposomes were removed. To afford the final two-layer lipid structure, an anionic liposome (10% DOPC/20% DPPG/70% DPPC, in mole fraction) was added onto the hybrid bilayer and incubated for 1 h. The unattached liposomes were once again removed by thorough buffer exchange. To further stabilize the final lipid assemblies, thus-prepared samples were fixed in a mixture of 4% paraformaldehyde and 1% glutaraldehyde in DI water for 1 h. The fixative solution was subsequently exchanged out by DI water. Right before an AFM measurement, the remaining water covering the lipid complexes was gently blotted away with a paper towel.

Lipid samples probed in a fluid were prepared on glass substrates, similar to the procedure described above. Briefly, glass cover slides (Corning, USA) were first sonicated in acetone for 5 min, rinsed with DI water, and then boiled in the base piranha solution ($\text{NH}_3\cdot\text{H}_2\text{O}/30\% \text{H}_2\text{O}_2/\text{DI water}$, 1:1:5, v/v) for 30 min. After being rinsed with DI water again and dried with nitrogen, these glass substrates were mounted onto the magnetic sample support disks of the microscope with a double-sided adhesive tape. From there, the first cationic lipid bilayer on glass was prepared by adding a suitable amount of DOTAP/DOPC liposome solution (2/8, in mole fraction) onto the glass substrate followed by a 2 h incubation. After the removal of the unbound liposomes, the resulting lipid bilayer was further incubated in the second, anionic liposome solution (Rho-DPPE/DPPG/DPPC, 5/15/80, in mole fraction) for 1 h. The unbound liposomes were similarly removed by buffer exchange. Thus-prepared lipid structures were transferred onto the microscope scanning stage and assembled with a fluid cell (Bruker) to give a sealed and aqueous-immersed scanning environment.

The control AFM measurement shown in Figure S1C was carried out by dewetting¹⁸ the as-deposited lipid assemblies. To do this, lipid samples were briefly exposed to air by draining the HEPES buffer solution covering the samples from the fluid cells, which were immediately refilled with the same buffer to rehydrate the samples. Thus-treated lipid samples were then similarly probed by AFM in a fluid as described above.

Photoelectrochemical Measurements. The photoelectrochemical measurements were carried out in three-electrode Teflon photoelectrochemical cells consisting an ITO substrate covered with lipid nanoassemblies as the working electrode, a Pt wire as the counter electrode, and Ag/AgCl (in saturated KCl) as the reference electrode. All photocurrents were generated and collected under cell open-circuit potential conditions without an extra potential bias. For photocurrent generation, 50 mM ascorbate in HEPES buffer (10 mM HEPES, 100 mM NaCl, pH 7.70) was employed as the sacrificial electron donor. Oxygen in the cell was depleted by an enzymatic method reported elsewhere.^{7,19} To obtain photoaction spectra, photocells containing different lipid structures were illuminated with a 150 W xenon lamp (Ushio, Japan) whose wavelength selection was realized using a computer-controlled fluorescence spectrophotometer (RF-5301, Shimadzu, Japan). The resulting photocurrent was recorded on a PC-controlled potentiostat (CHI 910B, CH Instruments). The photoaction spectra reported in the main text have been corrected for nonuniform spectral distribution of excitation in 5 nm intervals using a silicon photometer (PM120, Thorlabs). The photon-to-electron quantum conversion efficiency (QE) was calculated at a maximum absorption wavelength of Rho-DPPE ($\lambda_m = 575 \text{ nm}$) using the equation, $\Phi = (i/e)/[(W\lambda_m/hc)(1 - 10^{-A})]$, where i is the measured photocurrent, e is the elementary charge, W is the light power at λ_m , h is Planck's constant, c is the light speed, and A is the absorbance of Rho-DPPE at λ_m in the final lipid assemblies.

RESULTS AND DISCUSSION

System Design. To capture the essence of the layered organization and energy flow in GSB, we designed a two-tier lipid nanoassembly, in which a layer of anionic unilamellar liposomes (average size: $\sim 80 \text{ nm}$) is electrostatically held on a

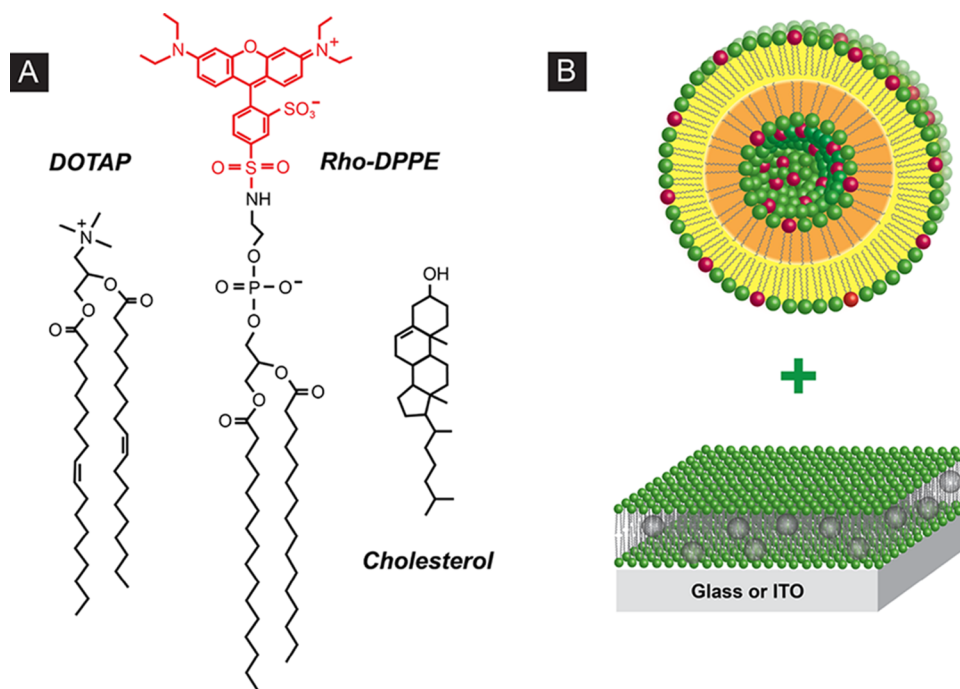


Figure 2. Main lipid components employed (A) in the formation of lipid-assembled photosynthetic mimics, which feature rhodamine and fullerene C₆₀ assembled in a liposome-on-lipid bilayer two-tier nanoassembly (B) bound electrostatically.

positively charged lipid bilayer (Figure 2B). At the beginning of this investigation, lipids comprising all-saturated C16 chains, such as DPPC and 1,2-dipalmitoyl-*sn*-glycero-3-phosphoglycerol (DPPG), were used to form the liposomes at the top. For the bottom lipid bilayer, unsaturated DOPC and cationic DOTAP were used. To provide light-harvesting capability to the lipid assembly, 5 mol % Lissamine rhodamine B conjugated to the phosphoethanolamine lipid (Rho-DPPE) was also incorporated into the top liposomes. Considering the ideal case in which lipids and dyes were symmetrically distributed between two identical leaflets of a spherical liposome, a loading of $\sim 3 \times 10^3$ rhodamines per liposome can be estimated.²⁰ Finally, to facilitate directional charge separation and electron transfer, 5% fullerene C₆₀ molecules as electron acceptors were further assembled into the underlying lipid bilayer.⁷ These supercomplexed lipid nanoassemblies were formed on either glass or ITO surfaces, and in the latter case, photocurrents can be directly generated and followed.

AFM of Lipid Deposits. Electrostatic deposition of charged liposomes on solid-supported lipid bilayers has been investigated previously,^{21–23} and the fact that no single final deposited structure emerges from these studies points to the complexity of such processes. Depending on the type of lipid, charge density, and other experimental variables (e.g., deposition time) employed, oppositely charged liposomes and bilayers may interact differently or to a different degree, giving rise to one or several distinct end features: intact liposomes on a lipid bilayer, lipid multilayers, and partial lipid exchange between the supported lipid bilayer and free liposomes.^{21–23} Although the first two cases produce morphological changes that can be identified by AFM, the detection of the third case requires other techniques such as fluorescence microscopy (next section).

As our initial attempt to unravel the morphology of electrostatically held lipid complexes, we used AFM to probe such assemblies in air. To maintain and reinforce the structure

thus formed in solution, the samples were first fixed with paraformaldehyde and glutaraldehyde before being exposed to air (see the Experimental Section). Besides the consideration on the relative ease of handling dry samples by AFM, the fixation step structurally locks everything in place and thus stops the deposited features from undergoing further morphological evolution. One such snapshot is shown in Figure 3A, revealing that individual liposomes can be deposited on a lipid bilayer in high density following our procedure. Although the measured average diameter of the liposomes is in line with that expected of the preparation, the height of these deposited features is much smaller: 5–15 nm. This deformation of spherical liposomes upon deposition and exposure to air very likely results from the alteration of forces, for example, electrostatic and hydration forces, experienced by each particle and in addition reflects the mechanical strength and conformability of cross-linked lipid bilayers.

We next moved to AFM measurements of aqueous-immersed lipid assemblies. Because these samples are prepared under conditions close to those employed in photocurrent generation (see the Experimental Section), that is, lipid composition and the microenvironment in which the lipid deposits are surrounded, images obtained here unveil the morphology of the latter more accurately. To our initial surprise, these measurements yielded features quite different from those collected in air. One representative image, shown in Figure 3B, discloses irregular-shaped lipid micropatches of 8–9 nm thickness, whose edges are occasionally decorated with particles sticking out 10–20 nm farther. These features indicate that the electrostatic interaction between the two lipid subunits causes large-scale liposome rupturing and spreading on the lipid bilayer, resulting in lipid multilayer formation and liposome adsorption. From time to time, smooth and almost featureless images were also obtained (Figure 3C), which may result from (1) the uneven distribution of lipid deposits and the limited area sampled by the AFM and (/or) (2) the rigid AFM tip

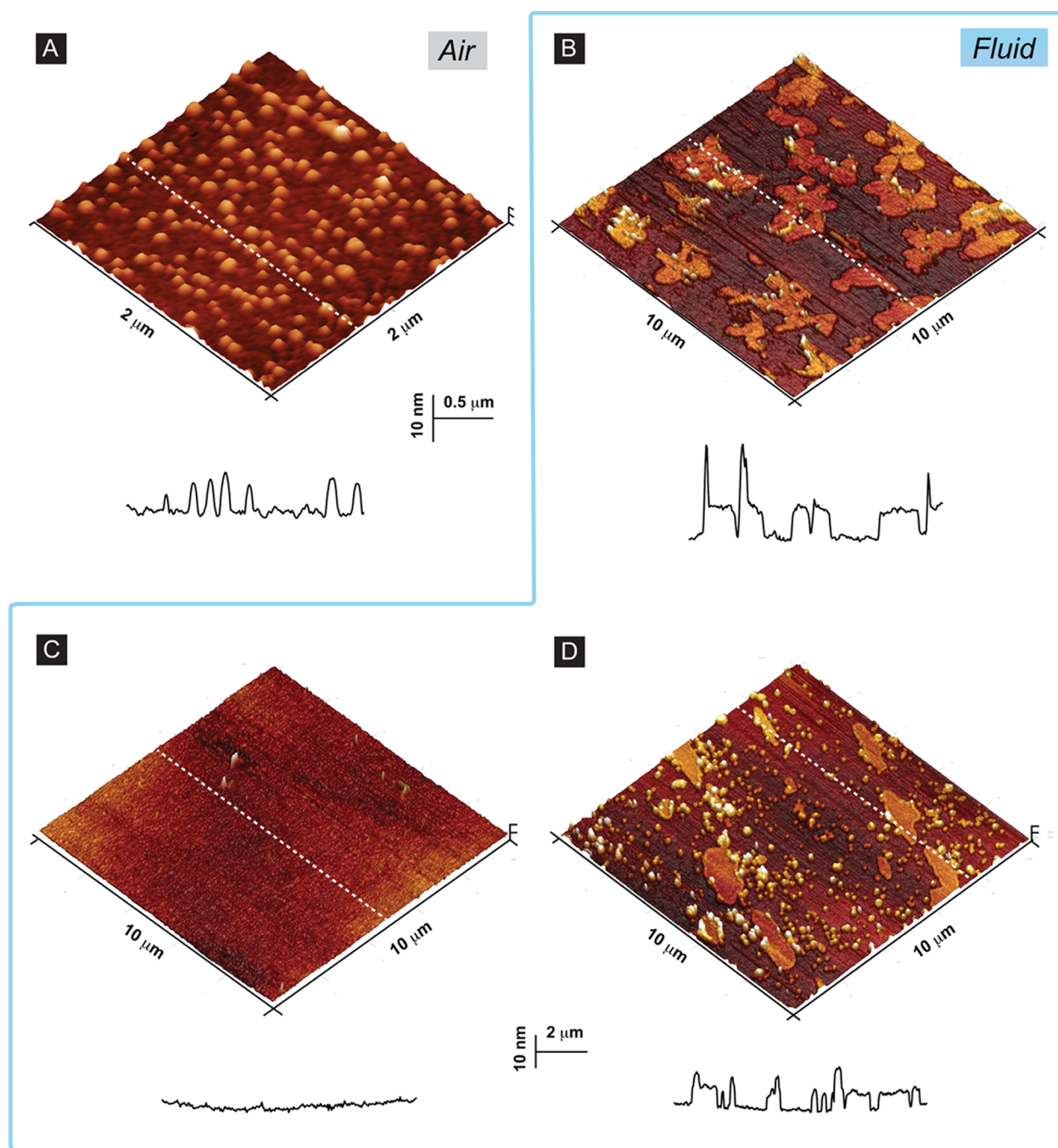


Figure 3. Structure of liposomes electrostatically deposited on lipid bilayers as probed by AFM. The image in (A) was obtained by scanning chemically fixed lipid assemblies in air on gold, whereas images (B)–(D) were lipid assemblies supported on glass and immersed in fluid (10 mM HEPES, 100 mM NaCl, pH 7.70). The height profiles shown at the bottom are obtained from line scans marked by the dashed lines in the corresponding images. Lipids employed to prepare liposomes: (A) DOPC/DPPG/DPPC (1/2/7 in mole fraction), (B) and (C) Rho-DPPE/DPPG/DPPC (5/15/80), and (D) DPPG/DPPC (2/8). The bottom lipid bilayer contains DOTAP/DOPC (2/8) in all cases. See the [Experimental Section](#) for more details.

pushing and distorting relatively soft lipid structures during scanning. It should also be noted that [Figure 3B,C](#) was obtained with liposomes containing an identical composition as that used in the photocurrent generation, including 5% Rho-DPPE. When the dye was omitted in the preparation, the most frequently encountered images recorded both individual liposome deposition and lipid spreading/fusion ([Figure 3D](#)). The height of micropatches obtained in this case is ~ 4 nm, which should correspond to a single lipid bilayer. This is very

different from [Figure 3B](#), where the micropatches are twice as thick on average, pointing to a plausible role of 5% Rho-DPPE in modifying the final structure. Taken together, these results provide us the first confirmation in this study that electrostatic interaction can be used to organize multiple lipid nanostructures into layered architectures.

Fluorescence Imaging. Imaging thus-formed lipid assemblies with confocal fluorescence microscopy further reveals that this protocol affords high-density liposome deposition across a

large surface area (Figure 4). Here, the most abundant fluorescent spots are formed by micron-sized lipid deposits,

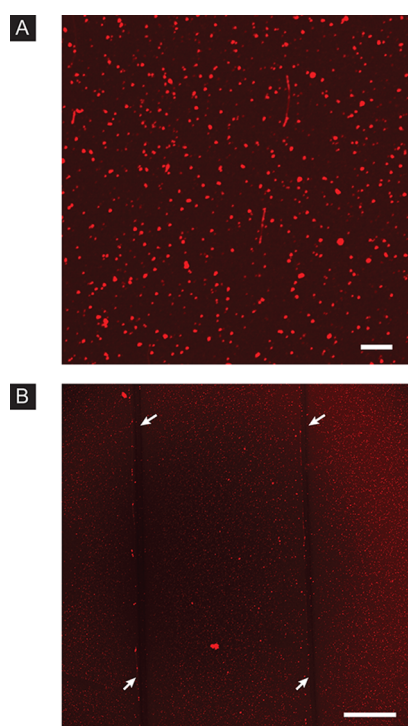


Figure 4. Fluorescence micrographs of rhodamine-labeled liposomes electrostatically deposited on an oppositely charged lipid bilayer supported on glass. Liposomes used: (A) Rho-DPPE/DPPG/DPPC (5/15/80) and (B) Rho-DPPE/DPPG/cholesterol/DPPC (5/15/30/50). White arrows in (B) point out the two passes where lipids were removed by scratching. The scale bars are (A) 10 and (B) 100 μm .

which should correspond to those micropatches resolved by AFM. Besides these prominent features, importantly, there exists a relatively uniform fluorescent background in all obtained images. As it is evident from Figure 4B, this fluorescence intensity is distinctly higher compared to the control dark background, where the lipid deposits are specifically removed by scratching. Because the AFM resolves only one major feature above the ground floor (i.e., micropatches) and the fluorescent Rho-DPPE is initially incorporated only into the liposomes to be deposited, this background fluorescence strongly suggests that lipid exchange has occurred between oppositely charged liposomes and the lipid bilayer during deposition.

Steady-State and Time-Resolved Fluorescence Spectroscopy. To assess the energy flow among rhodamine dyes and their electronic communication with fullerenes embedded in the lipid bilayer, we next characterized these layered lipid nanoassemblies using steady-state as well as time-resolved fluorescence spectroscopy. From steady-state fluorescence emission spectra, it was first found that the presence of 5% C_{60} in the bottom layer led to a 75% quenching of fluorescence emission from 5% Rho-DPPE in the DPPC/DPPG liposomes deposited atop (spectra in black and green, Figure 5 inset). Using time-resolved fluorescence spectroscopy, we further determined that the rhodamine sample without C_{60} coassembled and displayed two lifetimes at 0.73 and 2.41 ns, with amplitude weights of 62 and 38%, respectively. The lifetime of the long-lived component is close to the lifetime observed from

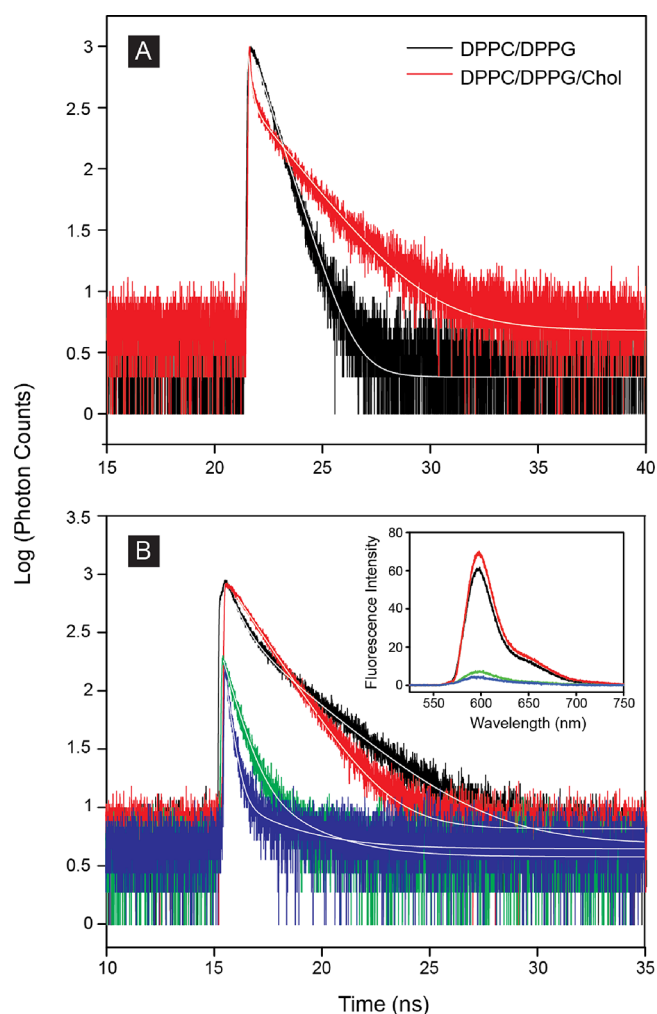


Figure 5. Steady-state and time-resolved fluorescence emission spectra of rhodamine assembled in liposome suspensions (A) and the two-layer lipid nanostructures (B). In (A), the liposomes, containing either DPPC/DPPG/Rho-DPPE (80/15/5) or DPPC/DPPG/cholesterol/Rho-DPPE (50/15/30/5), are dispersed in HEPES buffer, and the final rhodamine concentration is $\sim 0.5 \mu\text{M}$. All samples in (B) contain 5% Rho-DPPE and 15% DPPG in the top liposome layer. The complexes in addition contain 80% DPPC (black), 50% DPPC + 30% cholesterol (red), 80% DPPC + 5% C_{60} (in the bottom layer, traces in green), and 50% DPPC + 30% cholesterol + 5% C_{60} (blue). Exponential fitting curves associated with these decay profiles are shown by solid white lines embedded. The inset shows the corresponding steady-state fluorescence emission spectra of the four lipid deposits, which are color coded the same way. See the Experimental Section for more details.

the same dye/lipid conjugate via homogenous emission,²⁴ whereas the short-lived component most likely arises from self-quenching^{25,26} among the high-concentration and randomly distributed rhodamines existing in the gel-phase liposomes. Indeed, when the same sample was probed in the form of liposome suspensions instead of surface-deposited films, a single fluorescence lifetime of 0.79 ns was resolved. This result indicates that rhodamines exist in a relatively homogenous microenvironment in aqueous-dispersed liposomes and the dye loading in liposomes is high enough to induce global self-quenching. This lifetime is clearly of the same origin as the short component observed from the deposited sample, whereas their difference should result from changes in the liposome

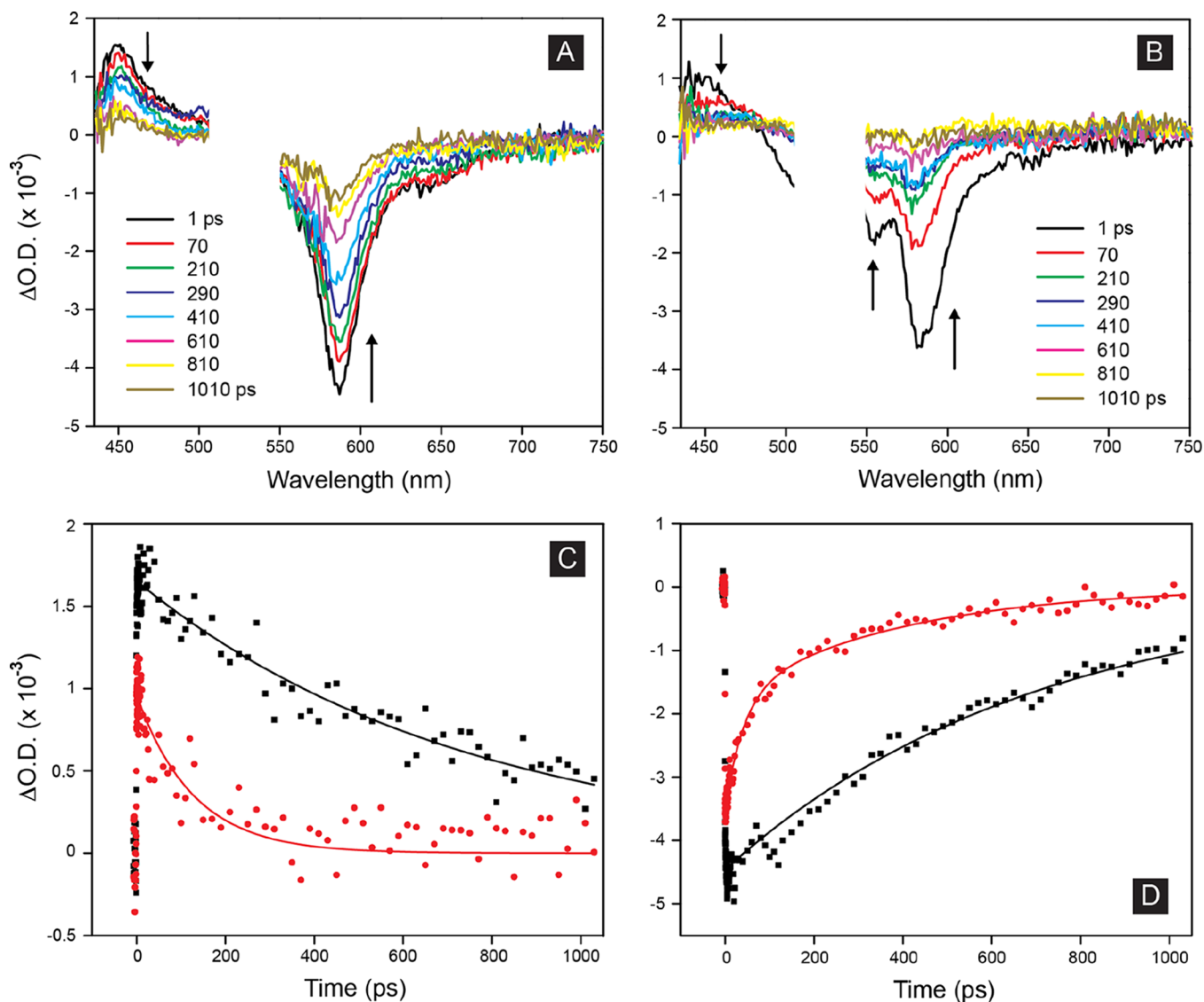


Figure 6. TA spectra of rhodamine in the liposome samples without (A) or with (B) cholesterol coassembled. Both samples contain 5% Rho-DPPE and 15% DPPG with the remaining portion(s) made up of 80% DPPC (A) or 50% DPPC + 30% cholesterol (B). The time-evolved optical density profiles at 450 (C) and 585 nm (D) of the cholesterol-containing and cholesterol-free samples are shown by red circles and black squares, respectively; the solid lines of the same color are the exponential fits of the experimental data.

morphology or rhodamine concentration upon deposition. Furthermore, considering these fluorescence decay behaviors together with fluorescence imaging data, it seems reasonable to assign the long decay component (2.41 ns) to be fluorescence emission by rhodamine dyes transferred from liposomes to the bottom lipid bilayer or recovered free emission due to dilution at the top layer. On the other hand, the addition of 5% C_{60} in the underlying lipid bilayer caused the otherwise similarly deposited rhodamines to fluoresce at lifetimes of 0.60 and 2.48 ns. Assuming that photoinduced electron transfer (PeT) between rhodamine and fullerene is the only additional pathway competing with fluorescence emission, a PeT rate constant of $6.1 \times 10^8 \text{ s}^{-1}$ can be obtained from $k_{\text{PeT}} = 1/\tau_{\text{F}(C_{60})} - 1/\tau_{\text{F}}$, where $1/\tau_{\text{F}(C_{60})}$ and $1/\tau_{\text{F}}$ are the measured fluorescence lifetime of rhodamine with and without fullerene, respectively. This rate constant compares well with those obtained from more frequently investigated porphyrin–fullerene conjugate complexes,^{27,28} thus verifying rhodamine dyes as a capable alternative electron-transfer partner to

fullerene. Together, these spectroscopic results evidence that an efficient electronic communication pathway exists between the assembled dye and fullerene populations, which are brought to close proximity by the electrostatically appressed lipid nanoassemblies.

TA Spectroscopy Characterization of Liposome Suspensions. The photodynamics of excited rhodamines in liposome suspensions were further probed by TA spectroscopy. As shown in Figure 6A, the TA spectra of rhodamine dyes in the liposome suspension display a negative absorbance band at 585 nm upon 150 fs pulse excitation, which corresponds to the ground-state bleaching and subsequent stimulated emission of excited rhodamine monomers. Concurrently, the TA spectra also display a positive absorbance band with a maximum at 450 nm, which should result from absorption by the excited-state rhodamines. Both of these spectral features have been previously observed for rhodamine dyes in solution or adsorbed on nanoparticles.²⁹ By fitting the kinetics of these features by

exponential functions, one can further determine the excited-state lifetime: 701 ps (at 585 nm) and 747 ps (at 450 nm).

Photocurrent Generation. As a direct test of the overall energy/electron transfer efficiency among all assembled components, these lipid supercomplexes were also wired to transparent ITO^{7,30} electrodes to produce photocurrent (see the [Experimental Section](#)). As shown in [Figure 7](#), for the

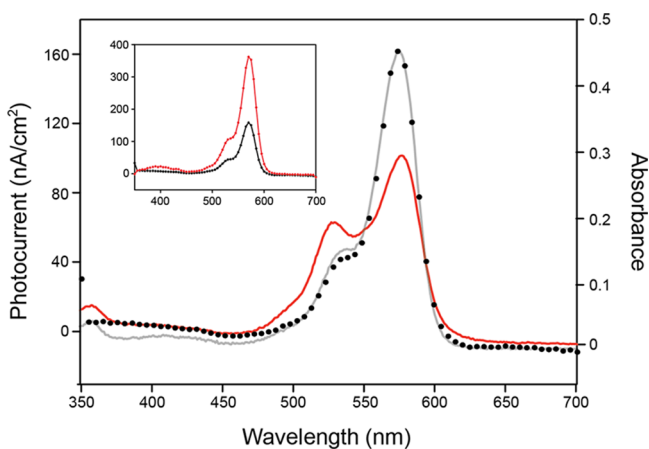


Figure 7. Absorption spectra of 5 mol % Rho-DPPE in liposomes in the presence (in red) or absence (in gray) of 30 mol % cholesterol. The rhodamine concentration in both samples is approximately 5 μM . The trace shown in solid circle is the corresponding photoaction spectrum of the cholesterol-free sample. Inset: photoaction spectra of lipid-assembled rhodamines/fullerenes with (in red) or without (in black) cholesterol; coordinates are identical to the main plot.

photocell containing 5% Rho-DPPE in the top liposome layer and 5% fullerene C_{60} in the lipid underlayer, the photoelectrochemical action spectrum tracks closely the electronic absorption of rhodamine, suggesting that rhodamine is primarily responsible for the light harvesting and an efficient PeT process exists between rhodamine and fullerene. The internal photon-to-electron QE is a very encouraging value of 7.8%. By contrast, photocurrents from cells containing 5% rhodamine alone are negligible, which indicates that effective charge separation can be achieved only when a suitable electron acceptor such as fullerene is also present in the assembly.

Performance Enhancement by Cholesterol. Further optimization of photoconversion efficiency has uncovered an intriguing role of the lipid matrix in influencing the distribution and organization of dyes in liposomes, which can significantly impact the ET dynamics and thus the performance of these lipid-assembled systems. Strikingly, when 30% cholesterol was added into the liposomes to replace DPPC, whereas other components were kept unchanged, the otherwise similarly configured photocell produced a QE of 14.2% (red trace, [Figure 7](#) inset).

To rule out the possibility that this enhanced performance is caused by some trivial mechanisms, for example, the addition of cholesterol in the top layer, facilitating fullerenes initially assembled underneath to enter the top layer and thus improving their electron transfer with rhodamines thereby, we also carried out additional control experiments. We found that, when the same amount of fullerenes was directly assembled into the liposomes (i.e., together with rhodamine and cholesterol) instead of the underlying lipid bilayer, the obtained QE was only 7.3%. This result, therefore, rejects the possibility of relocation of fullerenes (caused by cholesterol) as

the main mechanism of the observed enhancement. The significant difference in efficiency between these two cells highlights the delicacy of organizing an electron donor/acceptor into desired positions to achieve optimal performance and in addition suggests that rhodamine and fullerene remain largely associated with their lipid hosts during the photocurrent generation process. The latter conclusion was also reached in our previous study, where the same amphiphilic fullerene as used here was found to be able to maintain its position within individual leaflets (i.e., upper vs bottom half) comprising the same lipid bilayer.³¹

Cholesterol-Containing Systems: Fluorescence Imaging and AFM Characterization. To understand the underlying enhancement mechanisms, we next examined the liposome suspensions as well as liposome-on-bilayer assemblies containing cholesterol using AFM and various spectroscopic techniques. By comparing these with cholesterol-free samples, we hope to identify morphological and spectroscopic fingerprints that can be associated with the presence of this species in the lipid complexes.

Under the confocal fluorescence microscope, the electrostatically bound liposome (with 30% cholesterol)/lipid bilayer assemblies appear similar to their cholesterol-free counterparts, featuring micron-sized lipid deposits dispersed in a common fluorescence background ([Figure S1A](#)). This similarity is not unexpected as cholesterol, a neutral species, would not directly participate in the interaction process between oppositely charged lipids. On the other hand, our AFM measurements on cholesterol-containing deposits almost exclusively return images with no apparent features—similar to [Figure 3C](#). Only once out of about a dozen attempts were we able to resolve additional features on top of the flat background, which in this particular case suggests a deposition process based on intact individual liposomes ([Figure S1B](#)). Besides factors already mentioned, such as the uneven distribution of lipid deposits and the limited areas probed by the AFM, the elusiveness of well-resolved cholesterol-containing structures may be because of the fact that cholesterol can significantly increase the fluidity³² of the liposome lipid matrix, which is composed of lipids with all-saturated C16 chains. As such, these softened lipid deposits tend to be pushed aside by the AFM tip more easily during scanning and therefore are not captured in the final images. In a separate control experiment, finally, we also confirmed that these featureless samples are nevertheless covered by a lipid bilayer ([Figure S1C](#)).

Cholesterol-Containing Systems: Spectroscopic Characterization. Further spectroscopic characterization of rhodamine dyes in liposomes coassembled with cholesterol reveals several important new features. The first piece is from the ground-state absorption spectroscopy, where rhodamine dyes in the cholesterol-containing liposomes display a significantly intensified shoulder peak at the expense of the main 0–0 transition (red trace, [Figure 7](#)). An 8 nm shift toward the shorter wavelength can also be clearly discerned. In TA spectroscopy, the same sample displays an additional negative absorption band at 555 nm, which is absent for the liposome sample containing the same amount of rhodamine but no cholesterol ([Figure 6B](#)). The influence of cholesterol on the photodynamics of coassembled rhodamines is clearly evident by following the decay/recovery of these absorption maxima over time ([Figure 6C,D](#)). At 585 nm, a lifetime of 701 ps for rhodamines in cholesterol-free liposomes was found, whereas two time constants of 41 and 391 ps were obtained for the

Table 1. Excited-State Lifetimes of Rhodamines Assembled in Liposomes as Probed by Time-Correlated Fluorescence Single-Photon Counting (TCSPC) and TA Spectroscopy

lipid composition	fluorescence lifetime (ns) ^a	excited-state lifetime (ps) ^b		
		585 nm	450 nm	555 nm
Rho-DPPE/DPPC/DPPG: 5/80/15	0.79	701 ± 18	747 ± 25	
Rho-DPPE/DPPC/DPPG/Chol: 5/50/15/30	2.05 (41%), 0.21 (59%)	41 ± 5; 391 ± 29	127 ± 13	302 ± 12

^aData obtained from TCSPC measurements. ^bData obtained from TA measurements. See also Figures 5 and 6.

Table 2. Spectroscopic and Photoelectrochemical Characteristics of Rhodamines Assembled in Various Lipid Supercomplexes

lipid composition in the top liposome layer ^a	fluorescence lifetime (ns) ^b	k_{PeT} (s ⁻¹)	photoconversion QE (%)
Rho-DPPE/DPPC/DPPG: 5/80/15	0.73 (62%), 2.41 (38%) ^c (0.60 (92%), 2.48 (8%)) ^d	6.1 × 10 ⁸	7.8 (±0.6) ^e
Rho-DPPE/DPPC/DPPG/Chol: 5/50/15/30	1.60 ^c (0.26 (90%), 1.75 (10%)) ^d	1.9 × 10 ⁹	14.2 (±0.6)

^aAll bottom lipid bilayers contain DOPC/DOTAP in an 80/20 mixing ratio with/without five additional fractions of C₆₀. ^bData obtained from TCSPC measurements. ^cMeasured with dye alone. ^dWith C₆₀ coassembled. ^eStandard deviation, $n = 3$.

same dye in cholesterol-coassembled liposomes. Likewise, the lifetimes of the rhodamine dimers as judged by the absorbance change at 555 nm are found to be 302 ps. A similar trend is also obtained by fitting the data at 450 nm: 747 ps (no cholesterol) vs a much shorter 127 ps when cholesterol is coassembled. On the other hand, by probing the same liposome samples with time-resolved fluorescence spectroscopy, we identified a single fluorescence lifetime of 0.79 ns for the cholesterol-free sample and two lifetimes at 0.21 and 2.05 ns for the cholesterol-included sample. These time constants are in general agreement with those found by the TA spectroscopy, whereas the discrepancies are likely caused by the different time resolution and experimental setup, for example, the probed time window and photoexcitation conditions, between the two techniques.

When these cholesterol-containing liposomes are further deposited on a solid-supported lipid bilayer via electrostatic interactions, the photodynamics displayed by the coassembled rhodamines changed once again. Here, a single-component fluorescence lifetime of 1.60 ns was observed when the bilayer contained no electron-accepting fullerenes, whereas for the lipid complex with fullerene incorporated, the lifetime of the fluorophore was drastically shortened to 0.41 ns (amplitude-weighted average of two components). From these data, one can again estimate the rate constant of the competing PeT process, $1.9 \times 10^9 \text{ s}^{-1}$, which is more than two times faster compared to that of the cholesterol-free supercomplex. All photoelectrochemical and spectroscopic data associated with these two lipid complexes are summarized in Tables 1 and 2.

Cholesterol-Containing Systems: Discussion on Enhancement Mechanisms. How could the simple addition of cholesterol boost the photoconversion efficiency by >80% in these lipid supercomplexes? To answer this question, it is necessary to first delineate the relevant biophysical functions of this important molecule in biomembranes. A ubiquitous functional and structural component in biomembranes, cholesterol may contribute to the enhanced performance through several closely related mechanisms.^{32–34} Structurally, cholesterol features a rigid four-member fused ring connecting a hydroxyl group and a relatively flexible C6 hydrocarbon chain at its distal ends (Figure 2A). This arrangement renders the overall molecule amphiphilic³⁵ and an end-to-end length of about 2 nm when fully extended,³⁶ that is, about half of the thickness of a typical lipid bilayer. When juxtaposed with phospholipids, cholesterol forms hydrogen bonding with the

latter^{37,38} (i.e., between its OH group and the *sn*-2 carbonyl/phosphate oxygen of the latter), and its hydrocarbon portion is further associated with the acyl chains of the phospholipids via hydrophobic/hydrophobic interactions in both leaflets of the bilayer. Thanks to these specific interactions, cholesterol tends to insert into a lipid bilayer with a preferential orientation and at a fixed depth and in so doing can occupy biomembranes in very high concentrations, for example, ~50% in red blood cells.³³ Compared to typical phospholipids, moreover, cholesterol is compact in size and dissimilar in geometry, that is, a small hydrophilic OH headgroup relative to its hydrocarbon backbone. Broadly speaking, it is this unique combination of complexing ability and structural mismatch with phospholipids that renders cholesterol the universal molecular wedge/filler inside lipid membranes. As such, it modifies the ordering, packing density, and distribution of neighboring phospholipids, thereby impacting the physical and mechanical characteristics of the lipid membrane at a macroscopic level.^{33,34} Naturally, such modification effects come about in a lipid-, concentration- and temperature-dependent fashion. If the lipid bilayer is fluidic and disordered at room temperature to start with, for example, based on lipids with unsaturated acyl chains such as DOPC (18:1, two identical C18 chains with one double-bond each, phase-transition temperature, T_m , at $-17 \text{ }^\circ\text{C}$), adding cholesterol will increase the order of lipid organization, condense the lipid matrix, and thus lower the fluidity of the resulting membrane.^{39,40} On the contrary, for a bilayer existing in the ordered gel phase at room temperature, for example, DPPC (16:0, $T_m = 41 \text{ }^\circ\text{C}$), incorporating cholesterol will not only increase the lipid ordering further but also help to break up the rigid lipid network, thus producing a more fluidic lipid bilayer.^{41,42} In both cases, such ordering/condensing effects kick in first locally at low cholesterol concentrations, which effectively generate heterogeneity within the lipid matrix and hence phase separation.^{43–45} Conceivably, as cholesterol interacts with different lipids (with various headgroups and acyl chains) differently and such interactions are also concentration dependent, the phase behavior of multi-component lipid matrices can be quite complex.⁴⁶

Back to our system and consider the rhodamine-assembled liposome suspensions first. Due mainly to the common 16:0 chains, Rho-DPPE lipids distribute homogeneously in the gel-phase DPPC/DPPG matrix⁴⁷ at room temperature.⁵¹ At a high dye loading of 5%, rhodamines in the same liposome host are

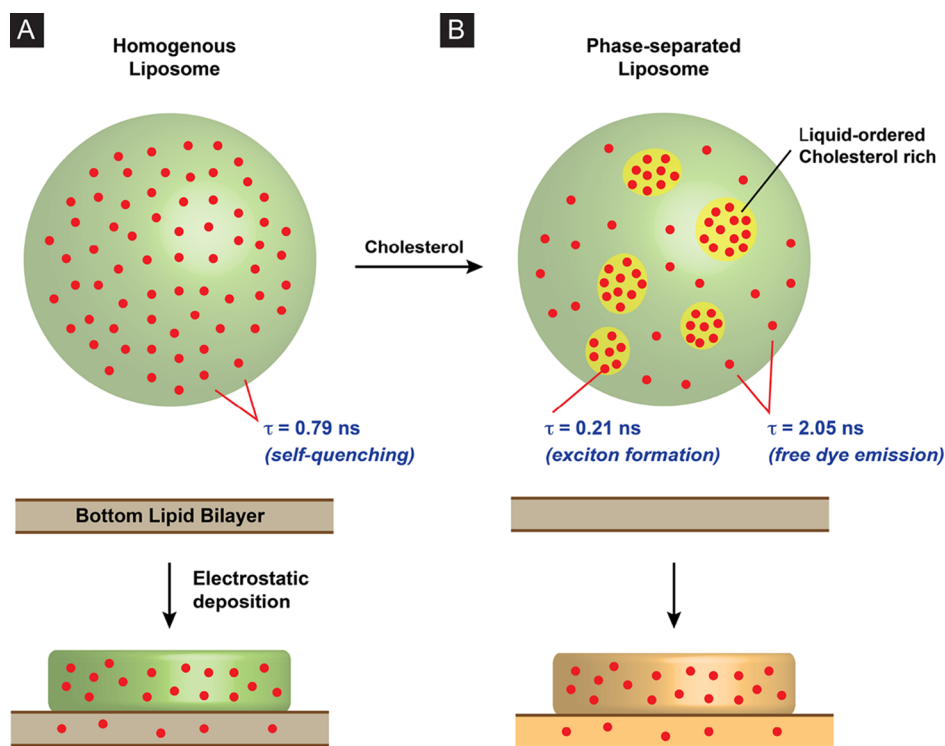


Figure 8. Cartoon depiction of cholesterol-induced phase separation (gel vs liquid-ordered phase) in liposomes and the clustering of rhodamine dyes in the cholesterol-rich liquid-ordered phase. Objects are color coded in terms of lipid composition; red dots represent individual rhodamine molecules. These drawings grant no information regarding the dye cluster size, distribution, or number of dyes per cluster in liposomes.

placed within a direct electronic-coupling distance with their neighbors. However, because all three lipids still maintain freedom to rotate about the bilayer normal,³³ there exists no apparent order in relative orientation among rhodamines, and as a result, such a coupling only leads to destructive self-quenching via ET between excited- and ground-state dyes. This is first evidenced by a single fluorescence lifetime (0.79 ns) that is much shorter than that of free-emitting individual dyes, for example, ~ 2.4 ns. When 30% cholesterol is included in the DPPC/DPPG (50/15%) liposomes, the pure gel-phase matrix of the latter is partially replaced by a new liquid-ordered phase modulated by cholesterol, resulting in two-phase coexistence.^{52,53} Of the two, the coassembled rhodamine prefers the new phase, which may be driven by its direct participation in the hydrogen-bonding network. In a fluorescence lifetime imaging microscopy study of DPPC/cholesterol vesicles, de Almeida et al. previously identified a preferential partition of rhodamine conjugated to dioleoylphosphatidylethanolamine (DOPE, 18:1) into the liquid-ordered phase over the gel phase.⁵⁴ Without the double bonds disrupting the association among lipid hydrocarbon chains in the present system, this preferential partition is expected to be even stronger. This produces two net effects: clustering of dyes in the cholesterol-rich domain and a concentration decrease of dyes remaining associated with the gel phase (Figure 8). Situated in different microenvironments, the photodynamics of these two rhodamine populations diverge. For those dyes existing in the gel phase, a lower concentration means greater dye-to-dye separation and less coupling and self-quenching; therefore, their fluorescence lifetime recovers and approaches that of undisturbed emission from individual dyes. In comparison, the situation is more complex for those rhodamines in the liquid-ordered phase. Here, the dyes are not only crowded (hence a

shortened dye-to-dye distance) but, because the presence of cholesterol further reduces the tilting of lipids versus the bilayer normal and hence the cross-sectional area occupied per lipid,^{33,34,42–44} it also modifies the relative orientation of transition dipoles among rhodamines. As a result, these dyes respond to the light excitation *collectively*, producing exciton states that display very different photodynamics compared to those of individual dye molecules.

The spectroscopic evidence presented above directly points to exciton formation in dye aggregates when cholesterol is coassembled in these lipid nanoassemblies. In particular, the shoulder peak observed in both steady-state and TA spectra only when cholesterol is present can be attributed to rhodamine dimer formation, which has been observed previously in several types of rhodamine dye aggregates.^{55–57} Combining this feature with the blue-shifted 0–0 absorption band, it can be further deduced that the cholesterol-coassembled rhodamines belong to the weakly coupled exciton characteristic of H aggregates,^{58,59} that is, with the dye transition dipoles arranged in parallel. Considering the facts that the transition dipole of rhodamine oscillates along the long axis of the molecule defined by the xanthene backbone^{51,60} and a large distance (i.e., >4 nm) separates dyes occupying the opposite leaflets of the liposomal bilayer, this effective dimerization most likely results from an enhanced alignment of rhodamines within the same leaflet as cholesterol orders the neighboring lipids and limits their rotation therein. Consistent with this two-population analysis, the rhodamine/cholesterol-coassembled liposomes fluoresce in two lifetimes: 2.05 and 0.21 ns. The latter component may result from the faster ET between rhodamine monomers and dimers. Here, it is important to note that such a short fluorescence/excited-state lifetime cannot be obtained simply by crowding the rhodamines without cholesterol. As shown in

Table S1, when the dye concentration in liposomes was systematically increased, a monotonous decrease in the fluorescence lifetime was obtained, again because of greater self-quenching at higher concentrations. Of all concentrations examined, however, the rhodamines fluoresce in a single population. Even at an extremely high dye loading of 40%, the obtained lifetime remains significantly longer than that of cholesterol-containing samples, pointing once again to the critical roles of this species.

Complexing these liposomes with a solid-supported lipid bilayer further modifies the organization and lipid micro-environment in which the rhodamines reside and hence their photodynamics. As clearly evident from Figures 3 and 4, the electrostatic interaction between these two lipid assemblies causes the liposomes to rupture and spread on the oppositely charged bilayer, producing multilayer lipid micropatches. Accompanying this morphological transition, there is also lipid transfer, which can occur as soon as the liposomes start landing on the solid-supported bilayer. For the rhodamines assembled in DPPC/DPPG liposomes, this transfer process brings a new population of dyes into the bottom bilayer, which fluoresces relatively undisturbed, that is, 2.41 ns. For those dyes that remain associated with the original host, the fluorescence lifetime is almost unchanged: 0.73 vs 0.79 ns in suspended liposomes. In striking contrast, when liposomes containing 30% cholesterol were similarly deposited, only a single fluorescence lifetime of 1.60 ns was found. Because the fluorescence imaging identifies two dye locations (Figures 4B and S1A), that is, in the bilayer and micropatches, similar to cholesterol-free assemblies, this single-component emission suggests improved electronic communication among rhodamines as a result of their rearrangement upon lipid deposition. As mentioned above, cholesterol can order and condense both fluidic/disordered and gel/ordered lipid bilayers, leveling the fluidity and mechanical strength of the resulting membranes. When cholesterol-containing liposomes are being deposited on the solid-supported bilayer, not only will cholesterol enter the bilayer, but it will also facilitate the transfer of all other species in both directions. This large-scale transfer and mixing of lipids effectively demolishes the phase segregation in the liposomes, resulting in homogenization of dyes throughout the assembled network (Figure 8). In comparison, such a transfer would be considerably weaker in the absence of cholesterol because of mismatches in phase and mechanical characteristics between the two lipid nanoassemblies.

Finally, when the electron-accepting fullerene is also incorporated, the photodynamics of rhodamine dyes coexisting in the system change yet again as a result of PeT between the two. This efficient process opens up another energy-dissipation channel to the photoexcited dyes, which produces a shortened fluorescence lifetime accompanied by a low-population (~10%) long-lived component in both cases (Table 2). Interestingly, the latter component is even slightly longer than that observed in the corresponding fullerene-free lipid complexes, which indicates that the PeT process engages the majority but not all of the dyes. In consequence, for those rhodamines whose excited states elude direct electronic communication with fullerenes, their fluorescence emission recovers as the PeT relaxes their coupling with other dyes. One plausible assignment for such is the dye population located within liposomes decorating the edge of lipid micropatches (Figure 3B,D), which is separated the furthest from fullerenes embedded in the lipid bilayer underneath. Strikingly, with every other component/

factor held identical, the lipid complex with 30% cholesterol displays a PeT rate constant two times faster than that of the corresponding cholesterol-free system, which underpins the higher photoconversion efficiency observed in the former (Table 2). This result once again supports the notion that cholesterol can significantly enhance the electronic communication among rhodamine dyes coassembled, inducing the latter to behave collectively within the same supramolecular network. Throughout this network, this exciton-based transfer mechanism supersedes Förster-type energy hopping among individual dyes,^{61,62} facilitating a more efficient delivery of the harvested light energy to the charge-separation sites. Another potential contributor to the enhanced performance may be the condensed and more ordered medium, which would benefit the ET processes by lowering the extent of energy loss due to vibrations, that is, the electron–phonon coupling,^{63,64} within the lipid matrix. A good number of recent investigations have highlighted the general occurrence of exciton formation^{2,61} in photosynthetic complexes, which nature employs to fight off energy losses due to electron–phonon coupling and disorders in soft protein matrices. By this mechanism, for example, a higher level of coherence of excited states is achieved in the FMO protein,⁶⁵ and additional quantum-mechanical states are activated for ET and trapping in purple bacteria.⁶⁶

It is also important to note that the differences observed in the absorption spectra are absent in their corresponding photoaction spectra. As shown in Figure 7 inset, the lipid deposits with/without cholesterol display essentially identical photoaction profiles, that is, the peak position and relative intensity, despite that the photocurrent is more than tripled in the cholesterol-containing samples. These results indicate that, instead of the exciton states, it is the same first singlet excited state (S_1) of individual rhodamines that is directly responsible for the charge separation in both complexes. To account for this seemingly surprising disparity, one needs to realize the fact that only those dyes situated within the bilayer are close enough to the bilayer-embedded fullerenes to directly participate in the electron transfer with the latter. Although exciton formation speeds up ET within the cholesterol-containing deposits, the harvested light energy has to be first funneled to and collected by these interfacial rhodamines, and the subsequent charge separation events take place primarily between individual electron donors and acceptors. Thus, similar to their natural counterpart, for example, BChl pigments in GSB (Figure 1), these lipid-assembled rhodamine dyes can carry out either ET or charge separation depending on their location and surrounding partners in the photosynthetic machinery.

■ CONCLUDING REMARKS

Following nature's lead, we have developed multilayer lipid-assembled supercomplexes to mimic key steps in photosynthesis. Efficient PeT is identified between rhodamine and fullerene, which adds this class of dyes into the repository of small-molecule organic photovoltaics. The remarkable possibility of using a lipid matrix to improve photoconversion efficiency is further demonstrated by cholesterol, whose addition triggers exciton formation that leads to faster ET in these lipid nanoassemblies. Our approach should be immediately useful in designing new models to study the photodynamics of dye aggregates under quasi-natural settings. Constructed right, these systems should even be able to host or interface with natural photosynthetic components to interrogate photoelectrochemical properties of the latter or to

form hybrid photoconverting devices. Possibilities to further enhance the functionality and performance of these lipid-assembled supercomplexes are equally exciting. For instance, it should be possible to extend the current design by including multiple dyes to occupy different locations in the lipid matrix. Alternatively, additional lipid structures and layers can be introduced into these lipid assemblies for more efficient light harvesting and electronic excitation transfer. Some of these ideas are currently being explored in this laboratory.

■ ASSOCIATED CONTENT

● Supporting Information

The Supporting Information is available free of charge on the ACS Publications website at DOI: 10.1021/acs.langmuir.6b01608.

Fluorescence lifetime decay of rhodamine as a function of dye loading in cholesterol-free liposomes and fluorescence imaging and AFM characterization of cholesterol-incorporated liposomes electrostatically deposited on lipid bilayers (PDF)

■ AUTHOR INFORMATION

Corresponding Author

*E-mail: wzz0001@auburn.edu.

Present Address

§State Key Lab of Precision Spectroscopy, East China Normal University, Shanghai, China (J.C.).

Notes

The authors declare no competing financial interest.

■ ACKNOWLEDGMENTS

This work is supported by the National Science Foundation (CHE-0951743 to W.Z. and CHE-1309817 to T.L.).

■ REFERENCES

- (1) *Molecular Mechanisms of Photosynthesis*; Blankenship, R. E., Ed.; Blackwell Science Ltd.: Oxford, U.K., 2002.
- (2) Cheng, Y.-C.; Fleming, G. R. Dynamics of Light Harvesting in Photosynthesis. *Annu. Rev. Phys. Chem.* **2009**, *60*, 241–262.
- (3) Scholes, G. D.; Fleming, G. R.; Olaya-Castro, A.; van Grondelle, R. Lessons from Nature About Solar Light Harvesting. *Nat. Chem.* **2011**, *3*, 763–774.
- (4) Calvin, M. Simulating Photosynthetic Quantum Conversion. *Acc. Chem. Res.* **1978**, *11*, 369–374.
- (5) Gust, D.; Moore, T. A.; Moore, A. L. Mimicking Photosynthetic Solar Energy Transduction. *Acc. Chem. Res.* **2001**, *34*, 40–48.
- (6) Iida, K.; Nango, M.; Matsuura, M.; Yamaguchi, M.; Sato, K.; Tanaka, K.; Akimoto, K.; Yamashita, K.; Tsuda, K.; Kurono, Y. Energy Transfer and Electron Transfer of Poly(Ethylene Glycol)-Linked Fluorinated Porphyrin Derivatives in Lipid Bilayers. *Langmuir* **1996**, *12*, 450–458.
- (7) Zhan, W.; Jiang, K. A Modular Photocurrent Generation System Based on Phospholipid-Assembled Fullerenes. *Langmuir* **2008**, *24*, 13258–13261.
- (8) Lyman, S. V.; Parmon, V. N.; Zamaraev, K. I. Photoinduced Electron Transfer Across Membranes. *Top. Curr. Chem.* **1991**, *159*, 1–65.
- (9) Olson, J. M. Chlorophyll Organization and Function in Green Photosynthetic Bacteria. *Photochem. Photobiol.* **1998**, *67*, 61–75.
- (10) Frigaard, N.-U.; Chew, A. G. M.; Li, H.; Maresca, J. A.; Bryant, D. A. *Chlorobium tepidum*: Insights into the Structure, Physiology, and Metabolism of a Green Sulfur Bacterium Drived from the Complete Genome Sequence. *Photosynth. Res.* **2003**, *78*, 93–117.
- (11) Holzwarth, A. R.; Griebenow, K.; Schaffner, K. Chlorosomes, Photosynthetic Antennae with Novel Self-Organized Pigment Structures. *J. Photochem. Photobiol., A* **1992**, *65*, 61–71.
- (12) Oostergetel, G. T.; van Amerongen, H.; Boekema, E. J. The Chlorosome: A Prototype for Efficient Light Harvesting in Photosynthesis. *Photosynth. Res.* **2010**, *104*, 245–255.
- (13) Pedersen, M. Ø.; Linnanto, J.; Frigaard, N.-U.; Nielsen, N. C.; Miller, M. A Model of the Protein–Pigment Baseplate Complex in Chlorosomes of Photosynthetic Green Bacteria. *Photosynth. Res.* **2010**, *104*, 233–243.
- (14) Wen, J.; Zhang, H.; Gross, M. L.; Blankenship, R. E. Membrane Orientation of the FMO Antenna Protein from *Chlorobaculum tepidum* as Determined by Mass Spectrometry-Based Footprinting. *Proc. Natl. Acad. Sci. U.S.A.* **2009**, *106*, 6134–6139.
- (15) Tronrud, D. E.; Wen, J.; Gay, L.; Blankenship, R. E. The Structural Basis for the Difference in Absorbance Spectra for the FMO Antenna Protein from Various Green Sulfur Bacteria. *Photosynth. Res.* **2009**, *100*, 79–87.
- (16) Ben-Shem, A.; Frolow, F.; Nelson, N. Evolution of Photosystem I—From Symmetry through Pseudosymmetry to Asymmetry. *FEBS Lett.* **2004**, *564*, 274–280.
- (17) Jiang, K.; Xie, H.; Zhan, W. Photocurrent Generation from Ru(bpy)₃²⁺ Immobilized on Phospholipid/Alkanethiol Hybrid Bilayers. *Langmuir* **2009**, *25*, 11129–11136.
- (18) Attwood, S. J.; Choi, Y.; Leonenko, Z. Preparation of DOPC and DPPC Supported Planar Lipid Bilayers for Atomic Force Microscopy and Atomic Force Spectroscopy. *Int. J. Mol. Sci.* **2013**, *14*, 3514–3539.
- (19) Hwang, K. C.; Mauzerall, D. Photoinduced Electron Transport across a Lipid Bilayer Mediated by C₇₀. *Nature* **1993**, *361*, 138–140.
- (20) The estimate is obtained as follows. Total lipid area per liposome is twice $4 \times \pi \times (40)^2 \text{ nm}^2$, which is $\sim 40\,000 \text{ nm}^2$. This area corresponds to $\sim 57\,000$ lipid molecules, approximated using the area occupied per DPPC in a bilayer, 0.7 nm^2 . Factoring in the dye loading, 5%, then gives the number in the main text.
- (21) Liu, J.; Jiang, X.; Ashley, C.; Brinker, C. J. Electrostatically Mediated Liposome Fusion and Lipid Exchange with a Nanoparticle-Supported Bilayer for Control of Surface Charge, Drug Containment, and Delivery. *J. Am. Chem. Soc.* **2009**, *131*, 7567–7569.
- (22) Akita, H.; Kudo, A.; Minoura, A.; Yamaguti, M.; Khalil, I. A.; Moriguchi, R.; Masuda, T.; Danev, R.; Nagayama, K.; Kogure, K.; Harashima, H. Multi-Layered Nanoparticles for Penetrating the Endosome and Nuclear Membrane via a Step-Wise Membrane Fusion Process. *Biomaterials* **2009**, *30*, 2940–2949.
- (23) Solon, J.; Streicher, P.; Richter, R.; Brochard-Wyart, F.; Bassereau, P. Vesicles Surfing on a Lipid Bilayer: Self-Induced Haptotactic Motion. *Proc. Natl. Acad. Sci. U.S.A.* **2006**, *103*, 12382–12387.
- (24) Gadella, T. W. J., Jr.; Jovin, T. M.; Clegg, R. M. Fluorescence Lifetime Imaging Microscopy (FLIM): Spatial Resolution of Microstructures on the Nanosecond Time Scale. *Biophys. Chem.* **1993**, *48*, 221–239.
- (25) MacDonald, R. I. Characteristics of Self-quenching of the Fluorescence of Lipid-conjugated Rhodamine in Membranes. *J. Bio. Chem.* **1990**, *265*, 13533–13539.
- (26) Castro, B. M.; de Almeida, R. F. M.; Fedorov, A.; Prieto, M. The Photophysics of a Rhodamine Head Labeled Phospholipid in the Identification and Characterization of Membrane Lipid Phases. *Chem. Phys. Lipids* **2012**, *165*, 311–319.
- (27) Yamada, H.; Imahori, H.; Nishimura, Y.; Yamazaki, I.; Ahn, T. K.; Kim, S. K.; Kim, D.; Fukuzumi, S. Photovoltaic Properties of Self-Assembled Monolayers of Porphyrins and Porphyrin–Fullerene Dyads on ITO and Gold Surfaces. *J. Am. Chem. Soc.* **2003**, *125*, 9129–9139.
- (28) D’Souza, F.; Chitta, R.; Gadde, S.; Shafiqul Islam, D.-M.; Schumacher, A. L.; Zandler, M. E.; Araki, Y.; Ito, O. Design and Studies on Supramolecular Ferrocene–Porphyrin–Fullerene Constructs for Generating Long-Lived Charge Separated States. *J. Phys. Chem. B* **2006**, *110*, 25240–25250.

- (29) Huang, J.; Stockwell, D.; Boulesbaa, A.; Guo, J.; Lian, T. Comparison of Electron Injection Dynamics from Rhodamine B to In_2O_3 , SnO_2 , and ZnO Nanocrystalline Thin Films. *J. Phys. Chem. C* **2008**, *112*, 5203–5212.
- (30) Salafsky, J.; Groves, J. T.; Boxer, S. G. Architecture and Function of Membrane Proteins in Planar Supported Bilayers: A Study with Photosynthetic Reaction Centers. *Biochemistry* **1996**, *35*, 14773–14781.
- (31) Zhan, W.; Jiang, K.; Smith, M. D.; Bostic, H. E.; Best, M. D.; Auad, M. L.; Ruppel, J. V.; Kim, C.; Zhang, X. P. Photocurrent Generation from Porphyrin/Fullerene Complexes Assembled in a Tethered Lipid Bilayer. *Langmuir* **2010**, *26*, 15671–15679.
- (32) *Liposomes: A Practical Approach*; New, R. R. C., Ed.; IRL Press: Oxford, U.K., 1990.
- (33) Róg, T.; Pasenkiewicz-Gierula, M.; Vattulainen, I.; Karttunen, M. Ordering Effects of Cholesterol and Its Analogues. *Biochim. Biophys. Acta, Biomembr.* **2009**, *1788*, 97–121.
- (34) Hofstätter, C.; Lindahl, E.; Edholm, O. Molecular Dynamics Simulations of Phospholipid Bilayers with Cholesterol. *Biophys. J.* **2003**, *84*, 2192–2206.
- (35) Yeagle, P. L. Cholesterol and the Cell Membrane. *Biochim. Biophys. Acta, Rev. Bioenerg.* **1985**, *822*, 267–287.
- (36) Craven, B. M. Crystal Structure of Cholesterol Monohydrate. *Nature* **1976**, *260*, 727–729.
- (37) Sankaram, M. B.; Thompson, T. E. Modulation of Phospholipid Acyl Chain Order by Cholesterol. A Solid-State Deuterium Nuclear Magnetic Resonance Study. *Biochemistry* **1990**, *29*, 10676–10684.
- (38) Reinl, H.; Brumm, T.; Bayerl, T. M. Changes of the Physical Properties of the Liquid-Ordered Phase with Temperature in Binary Mixtures of DPPC with Cholesterol. *Biophys. J.* **1992**, *61*, 1025–1035.
- (39) Ho, C.; Slater, S. J.; Stubbs, C. D. Hydration and Order in Lipid Bilayers. *Biochemistry* **1995**, *34*, 6188–6195.
- (40) Alwarawrah, M.; Dai, J.; Huang, J. A Molecular View of the Cholesterol Condensing Effect in DOPC Lipid Bilayers. *J. Phys. Chem. B* **2010**, *114*, 7516–7523.
- (41) McIntosh, T. J. The Effect of Cholesterol on the Structure of Phosphatidylcholine Bilayers. *Biochim. Biophys. Acta, Biomembr.* **1978**, *513*, 43–58.
- (42) Chiu, S. W.; Jakobsson, E.; Mashl, R. J.; Scott, H. L. Cholesterol-Induced Modifications in Lipid Bilayers: A Simulation Study. *Biophys. J.* **2002**, *83*, 1842–1853.
- (43) Marsh, D. Cholesterol-Induced Fluid Membrane Domains: A Compendium of Lipid-Raft Ternary Phase Diagrams. *Biochim. Biophys. Acta, Biomembr.* **2009**, *1788*, 2114–2123.
- (44) Vist, M. R.; Davis, J. H. Phase Equilibria of Cholesterol/Dipalmitoylphosphatidylcholine Mixtures: Deuterium Nuclear Magnetic Resonance and Differential Scanning Calorimetry. *Biochemistry* **1990**, *29*, 451–464.
- (45) Sankaram, M. B.; Thompson, T. E. Cholesterol-Induced Fluid-Phase Immiscibility in Membranes. *Proc. Natl. Acad. Sci. U.S.A.* **1991**, *88*, 8686–8690.
- (46) Veatch, S. L.; Keller, S. L. Seeing Spots: Complex Phase Behavior in Simple Membranes. *Biochim. Biophys. Acta, Mol. Cell Res.* **2005**, *1746*, 172–185.
- (47) DPPG displays very similar phase behavior as DPPC when coexisting with the latter, e.g., refs 48–50.
- (48) Singh, H.; Emberley, J.; Morrow, M. R. Pressure Induces Interdigitation Differently in DPPC and DPPG. *Eur. Biophys. J.* **2008**, *37*, 783–792.
- (49) Blosser, M. C.; Starr, J. B.; Turtle, C. W.; Ashcraft, J.; Keller, S. L. Minimal Effect of Lipid Charge on Membrane Miscibility Phase Behavior in Three Ternary Systems. *Biophys. J.* **2013**, *104*, 2629–2638.
- (50) Mukai, M.; Regen, S. L. Exchangeable Mimics of DPPC and DPPG Exhibiting Similar Nearest-Neighbor Interactions in Fluid Bilayers. *Langmuir* **2015**, *31*, 12674–12678.
- (51) Bagatolli, L. A.; Gratton, E. Two Photon Fluorescence Microscopy of Coexisting Lipid Domains in Giant Unilamellar Vesicles of Binary Phospholipid Mixtures. *Biophys. J.* **2000**, *78*, 290–305.
- (52) Veatch, S. L.; Soubias, O.; Keller, S. L.; Gawrisch, K. Critical Fluctuations in Domain-Forming Lipid Mixtures. *Proc. Natl. Acad. Sci. U.S.A.* **2007**, *104*, 17650–17655.
- (53) Davis, J. H.; Clair, J. J.; Juhasz, J. Phase Equilibria in DOPC/DPPC- d_{62} /Cholesterol Mixtures. *Biophys. J.* **2009**, *96*, 521–539.
- (54) de Almeida, R. F. M.; Borst, J.; Fedorov, A.; Prieto, M.; Visser, A. J. W. G. Complexity of Lipid Domains and Rafts in Giant Unilamellar Vesicles Revealed by Combining Imaging and Microscopic and Macroscopic Time-Resolved Fluorescence. *Biophys. J.* **2007**, *93*, 539–553.
- (55) Kemnitz, K.; Yoshihara, K. Entropy-Driven Dimerization of Xanthene Dyes in Nonpolar Solution and Temperature-Dependent Fluorescence Decay of Dimers. *J. Phys. Chem.* **1991**, *95*, 6095–6104.
- (56) Burghardt, T. P.; Lyke, J. E.; Ajtai, K. Fluorescence Emission and Anisotropy from Rhodamine Dimers. *Biophys. Chem.* **1996**, *59*, 119–131.
- (57) Blackman, M. J.; Corrie, J. E. T.; Croney, J. C.; Kelly, G.; Eccleston, J. F.; Jameson, D. M. Structural and Biochemical Characterization of a Fluorogenic Rhodamine-Labeled Malarial Protease Substrate. *Biochemistry* **2002**, *41*, 12244–12252.
- (58) Kasha, M. Energy Transfer Mechanisms and the Molecular Exciton Model for Molecular Aggregates. *Radiat. Res.* **1963**, *20*, 55–70.
- (59) Spano, F. C. The Spectral Signatures of Frenkel Polarons in H- and J-Aggregates. *Acc. Chem. Res.* **2010**, *43*, 429–439.
- (60) Bogen, S.-T.; Karolin, J.; Molotkovsky, J. G.; Johansson, L. B.-Å. 1,32-Dihydroxy-Dotriacontane-bis(Rhodamine) 101 Ester. *J. Chem. Soc., Faraday Trans.* **1998**, *94*, 2435–2440.
- (61) Scholes, G. D. Designing Light-Harvesting Antenna Systems Based on Superradiant Molecular Aggregates. *Chem. Phys.* **2002**, *275*, 373–386.
- (62) Brandes, T. Coherent and Collective Quantum Optical Effects in Mesoscopic Systems. *Phys. Rep.* **2005**, *408*, 315–474.
- (63) Seifert, U. Configurations of Fluid Membranes and Vesicles. *Adv. Phys.* **1997**, *46*, 13–137.
- (64) Coropceanu, V.; Cornil, J.; da Silva Filho, D. A.; Olivier, Y.; Silbey, R.; Brédas, J.-L. Charge Transport in Organic Semiconductors. *Chem. Rev.* **2007**, *107*, 926–952.
- (65) Cho, M.; Vaswani, H. M.; Brixner, T.; Stenger, J.; Fleming, G. R. Exciton Analysis in 2D Electronic Spectroscopy. *J. Phys. Chem. B* **2005**, *109*, 10542–10556.
- (66) Cogdell, R. J.; Gall, A.; Köhler, J. The Architecture and Function of the Light-Harvesting Apparatus of Purple Bacteria: From Single Molecules to In Vivo Membranes. *Q. Rev. Biophys.* **2006**, *39*, 227–324.